JOURNAL OF SPACECRAFT AND ROCKETS
Vol. 38, No. 2, March–April 2001

Unsteady Flow Separation Can Endanger the Structural Integrity of Aerospace Launch Vehicles

Lars E. Ericsson*
Mountain View, California 94040

When during the ascent through the Earth's atmosphere the structural response of an aerospace launch vehicle changes from the usually benign case of the buffet response to wind gusts and air turbulence to the self-excited type, the response amplitude increases dramatically and could often endanger the structural integrity of the launch vehicle. This is what occurs when the structural response starts to interact with and modify the unsteady separated flow characteristics, which generates aerodynamic negative damping or undamping of the low-frequency bending modes. A literature survey has been performed to document how this condition has affected the various aerospace vehicles launched since the early 1960s. The developed analytic means, described in the referenced publications, can predict the worst-case vehicle response with the accuracy needed for preliminary design, provided that sufficiently detailed static aerodynamic data are available. The purpose is to help the design engineer determine whether any of the described flow phenomena that have been experienced by earlier launch vehicles could possibly occur on the new launch vehicle design, in which case the recommended analysis described in full detail in the referenced publications would need to be performed.

Nomenclature

A	=	axial force, coefficient $C_A = A/q_\infty(\pi d^2/4)$
C_σ	=	buffet response amplitude (Fig. 16c)
c	=	reference length, d
d	=	maximum nose diameter
L_N	=	hammerhead cylinder length (Fig. 16a)
M	=	Mach number
M_{dyn}	=	dynamic bending moment (Fig. 13)
M_{stat}	=	static bending moment (Fig. 13)
m	=	pitching moment, coefficient $C_m = m/q_\infty(\pi d^3/4)$
N	=	normal force, coefficient $C_N = N/q_\infty(\pi d^2/4)$
p	=	static pressure, coefficient $C_p = (p - p_\infty)/q_\infty$
q_∞	=	dynamic pressure, $\rho_\infty U_\infty^2/2$
t	=	time
U_∞	=	freestream velocity
$\bar{U}$	=	mean convection velocity; Eq. (3)
x	=	axial coordinate (Fig. 6)
$\dot{Z}$	=	translatory (sink) velocity of the center of gravity
α	=	angle of attack
$\bar{\alpha}$	=	generalized angle of attack; Eq. (4)
β	=	escape-rocket-wake translation effect (Fig. 7)
Δ	=	amplitude or increment
$\Delta^i C_N$	=	separation-induced normal force
$\Delta\theta_N$	=	oscillation amplitude at the nose tip
ζ_a	=	attached-flow aerodynamic damping as a fraction of critical damping
ζ_s	=	separation-induced aerodynamic damping as a fraction of critical damping
ζ_0	=	structural damping as a fraction of critical damping
θ	=	pitch perturbation
θ_c	=	semi-angle of nose cone
ν	=	Prandtl–Meyer expansion angle
ξ	=	dimensionless x coordinate, $(x - x_N)/c$ (Fig. 10)
ρ	=	air density
ϕ	=	mode deflection coordinate (Figs. 16, 21, and 22)

Subscripts

a	=	attached flow
cg	=	center of gravity or rotation axis
crit	=	critical
e	=	boundary-layer edge
N	=	nose
s	=	separated flow
∞	=	freestream conditions

Derivatives

$C_{m\theta}$	=	$\partial C_m/\partial\theta$; $C_m\dot{\theta} = \partial C_m/\partial(\dot{\theta}c/U_\infty)$
$C_{N\alpha}$	=	$\partial C_N/\partial\alpha$; $\Delta^i C_{N\alpha s}$, $\Delta^i C_{N\theta s}$, and $\Delta^i C_{N\beta s}$ defined in Fig. 7

Received 9 June 2000; revision received 26 October 2000; accepted for publication 8 November 2000.

*Engineering Consultant, 1518 Fordham Way. Fellow AIAA.

Introduction

DURING the ascent through the Earth's atmosphere, the payload shrouds of aerospace launch vehicles experience flow separation at transonic speeds, which generates fluctuating pressures of significant magnitude.[1] Until the early 1960s the structural oscillations in the low-frequency bending modes was computed as the buffet response to the pressure fluctuations. It could be shown that the reason for the failure of this type of analysis to predict the loss of the Able IV payload was that the structural response to the separation-induced forcing function modified the unsteady aerodynamics.[2,3] This feedback mechanism was provided by the shock-induced flow separation on the shallow boattail[4] (Fig. 1). During the bending oscillation, an undamping lift hysteresis is generated by convective flowfield time-lag effects.[5,6] At a certain angle of attack, the shock-induced flow separation (on the top side) will be located farther aft for increasing α than in the static case, which generates a dynamic lift increase that drives the bending motion. Conversely, for decreasing α, the shock will be located farther forward, which generates a lift decrease that also drives the bending oscillation. As expected, most of the bending response to the undamping force on the boattail of a hammerhead payload is generated by the first bending mode.[3] It is typical that one bending mode generates the dominant part of the elastic vehicle response to the undamping aerodynamic forces. However, it is not always the first bending mode. In the case of the Saturn-Apollo launch vehicle[7,8] (Fig. 2), it was the second bending mode that generated the critical response. In these cases, as well as in others to be discussed, flow separation provided the mechanism for the generation of aerodynamic undamping.

Background

The effect of separated flow on rigid-body vehicle dynamics was of great concern for the first generation of military reentry vehicles, as in the case of the Polaris reentry body at transonic speeds.[9,10] The damping measured in pitch oscillations showed the effects of

separated flow to be large and less than obvious[10] (Fig. 3). As the data for the 2-deg amplitude ($\Delta\theta = 2$ deg) showed large data scatter, it is understandable that measurements with a larger amplitude ($\Delta\theta = 6$ deg) were added to give a better definition of the aerodynamic damping derivative. The highly nonlinear separated-flow characteristics producing the experimental results in Fig. 3 are as follows.[9] At high subsonic speeds, the flow separation starts at the blunt-nose/cylinder shoulder (Fig. 4a). When the angle of attack is increased from $\alpha = 0$, the separated flow is swept to the leeward side, and the windward side rapidly approaches attached-flow conditions. The resulting aerodynamic forces are highly nonlinear, with static stability derivatives being one order of magnitude larger at $\alpha < 4$ deg than at $\alpha > 6$ deg, the latter being of roughly half the magnitude expected for attached flow conditions at $\alpha = 0$. At low supersonic speed (Fig. 4b), the flow is attached at $\alpha = 0$ and does not separate until a certain critical angle of attack α_s has been exceeded and the leeward side becomes fully separated. When the angle of attack is decreased, the flow does not reattach until $\alpha < \alpha_s$. This α hysteresis amplifies the undamping effect generated by the discontinuous increase of static stability[9] and accounts for the undamping measured at $0.95 \leq M \leq 1.2$ for $\Delta\theta = 6$ deg (Fig. 3). For the lower amplitude, $\Delta\theta = 2$ deg, oscillations around $\alpha_0 = 0$ did not produce the angle of attack needed to cause leeward side global flow separation (Fig. 4b). Consequently, the measured damping derivative at $M > 1.0$ was close to that expected for attached flow, for example, as represented by the shown slender body prediction in Fig. 3. At $M \leq 0.95$, increasing the amplitude from $\Delta\theta = 2$ to 6 deg permits the oscillations to include the α range from 4 to 6 deg, where the $C_m(\alpha)$ characteristics are relatively less affected by the nose-induced flow separation (Fig. 4a). This provides the damping contribution that distinguishes the data trend for $\Delta\theta = 6$ deg from that for $\Delta\theta = 2$ deg at $M \leq 0.95$ in Fig. 3.

Using pitching moment derivatives determined by static experiments the measured, large, adverse effects of flow separation on vehicle dynamics could be predicted when accounting for the effect of convective flow time lag[9,10] (Fig. 5). A typical characteristic of the effect of separated flow for the low frequencies of interest here is the opposite effect on dynamic and static stability generated by the convective-flow time-lag effect illustrated in the inset in Fig. 5. When the flare comes down to the position for $\alpha = 0$ at time t, it resides in the separated flowfield generated by the bluff nose at the

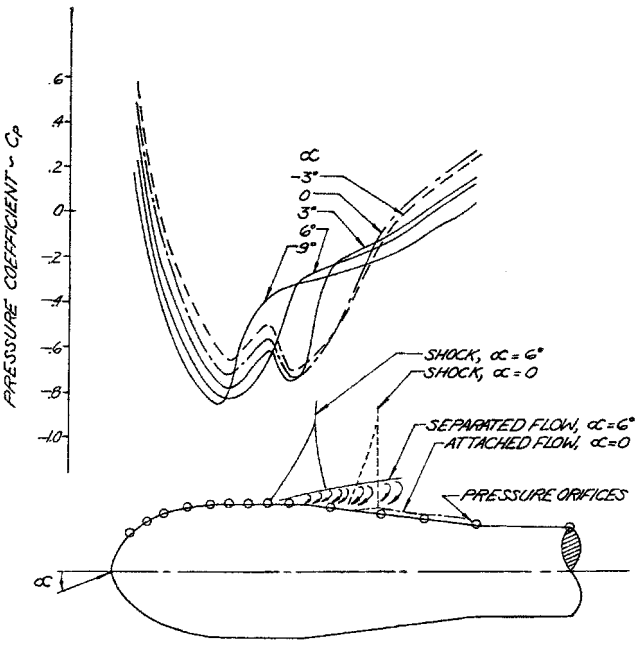

Fig. 1 Pressure distribution over the Able IV payload shroud at M = 0.95 (Ref. 4).

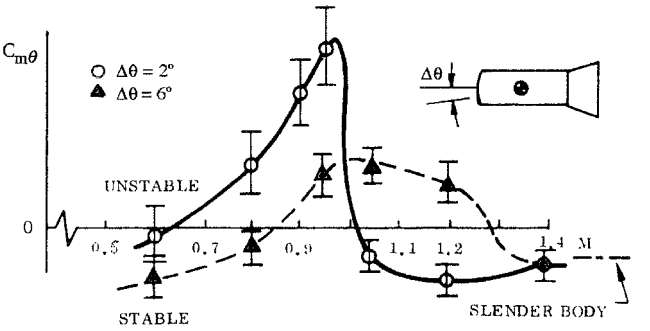

Fig. 3 Damping in pitch of Polaris reentry body.[10]

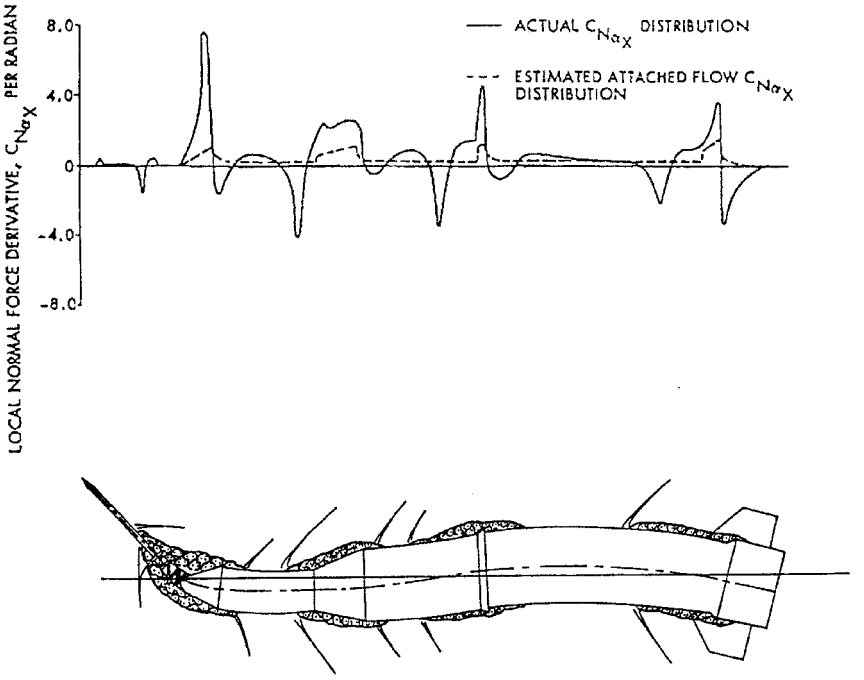

Fig. 2 Separated flowfield and associated normal force distribution at M = 1.2 on the Saturn–Apollo launch vehicle as it applies to the second bending mode.[7,8]

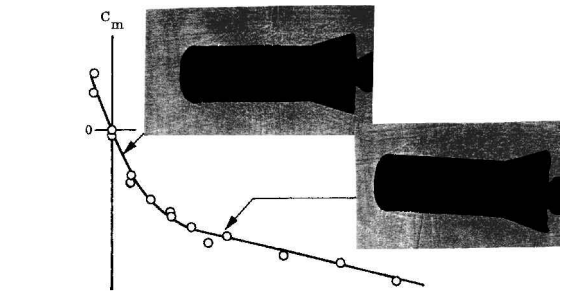

a) $M = 0.9$

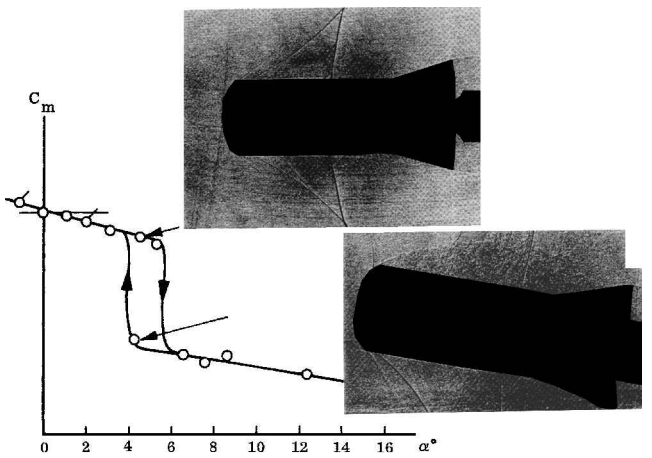

b) $M = 1.05$

Fig. 4 Transonic static aerodynamic characteristics of the Polaris reentry body.[9]

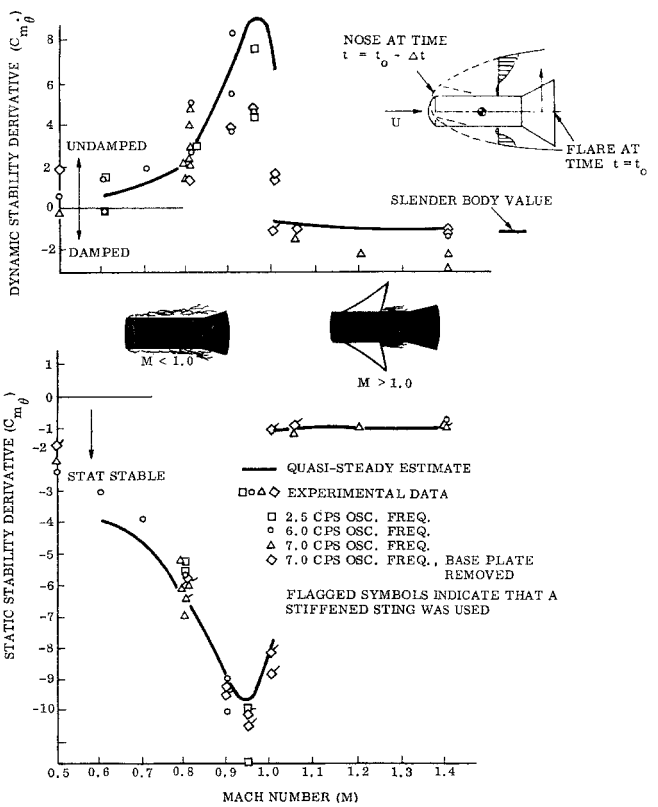

Fig. 5 Oscillatory moment derivatives of the Polaris reentry body for 1-deg ($\Delta\theta = 1$ deg) pitch oscillations around $\alpha = 0$ (Ref. 9).

earlier time instant $t - \Delta t$. The resulting residual flare force at $\alpha = 0$ drives the pitch rotation and, hence, is dynamically destabilizing, which explains the experimental results at $M \leq 1.0$ in Fig. 5. Note that, as will be demonstrated in the next section, in addition to reversing the statically stabilizing effect, the convective flow time lag also acts as an amplifier because the dynamic effect is proportional to the magnitude of the time lag.[9] Figure 5 shows that static experimental results can be used to predict the experimentally measured damping derivative with the accuracy needed for preliminary design. The analysis[9] leading to the prediction in Fig. 5 will be reviewed briefly to the extent it applies to the prediction of elastic vehicle dynamics. For a full analysis of the effect of separated flow on rigid and elastic vehicle dynamics, the reader is referred to Ref. 11.

Unsteady Aerodynamic Effects of Separated Flow

The separated flow characteristics generating the undamped oscillations in pitch at $\alpha = 0$ and $M \leq 1.0$ in Fig. 5 are shown in Fig. 6, which adds details to Fig. 5 that are needed to describe the analysis leading to the shown prediction of the pitch damping. Figure 6 shows how a change of the angle of attack from $\alpha = 0$ to θ changes the boundary of the nose-induced flow separation (see Fig. 4a). The resulting changes of the normal forces on the blunt nose and the circular cylinder are small and can be neglected in a first-order analysis. Consequently, only the separation-induced normal force N_s on the flare is of concern. It will be described here how N_s depends on the angles of attack α_N and α_s at x_N and x_s, respectively. The attitude α_N determines the lateral location of the shear flow at the flare, and α_s is the local attitude of the flare in the shear flow. The normal force N_s on the flare can be expressed as follows for small perturbations from α_N and α_s:

$$N_s = \left(\frac{\rho_\infty U_\infty^2}{2}\right)\left(\frac{\pi d^2}{2}\right)\left[\left(\frac{\partial C_{Ns}}{\partial \alpha_N}\right)\alpha_N + \left(\frac{\partial C_{Ns}}{\partial \alpha_s}\right)\alpha_s\right] \quad (1)$$

In the nonsteady case, the time history $\alpha_N(t)$ has to be considered. Its effect is represented in lumped form by the nose attitude at a discrete time increment Δt earlier than the instantaneous value. Thus, the flare normal force $N_s(t)$ can be written in the following form:

$$N_s(t) = \left(\frac{\rho_\infty U_\infty^2}{2}\right)\left(\frac{\pi d^2}{2}\right)\left[\left(\frac{\partial C_{Ns}}{\partial \alpha_N}\right)\alpha_N(t - \Delta t) + \left(\frac{\partial C_{Ns}}{\partial \alpha_s}\right)\alpha_s(t)\right] \quad (2)$$

where Δt is the time required for the shear flow at the flare to respond to the change of the angle of attack α_N. This time lag Δt is estimated as

$$\Delta t = \xi_s c/\bar{U} \quad (3a)$$

$$\bar{U}/U_\infty = [C_{As}/C_{Aa}]^{\frac{1}{2}} \quad (3b)$$

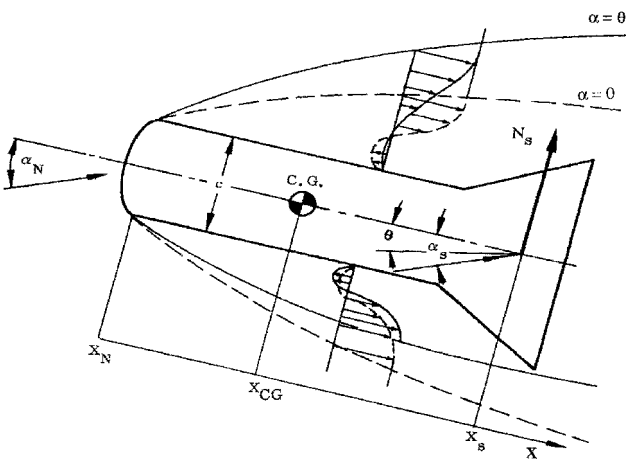

Fig. 6 Nose-induced separated flow characteristics on the Polaris reentry body.[9]

where C_{As} and C_{Aa} are the values of the flare forebody axial force measured in separated and attached flow, respectively.

The crossflow angle $\bar{\alpha}$ is

$$\bar{\alpha} = \alpha_0 + \theta + \dot{Z}/U_\infty \tag{4}$$

where α_0 is the time-averaged (trim) angle of attack and θ the body pitch perturbation.

Thus, for pitch oscillations around a fixed rotation axis at x_{cg} (Fig. 6), where $x - x_N = \xi c$, one obtains

$$\bar{\alpha}_s(t) = \alpha_0 + \theta(t) + (\xi_s - \xi_{cg})c\,\dot{\theta}/U_\infty \tag{5a}$$

$$\bar{\alpha}_N(t - \Delta t) = \alpha_0 + \theta(t - \Delta t) - \xi_{cg}c\,\dot{\theta}(t - \Delta t)/U_\infty \tag{5b}$$

For the slow oscillations of interest

$$\theta(t - \Delta t) \approx \theta(t) - \Delta t\dot{\theta}(t) \tag{6a}$$

$$\dot{\theta}(t - \Delta t) \approx \dot{\theta}(t) \tag{6b}$$

Combining Eqs. (3), (5), and (6) gives

$$\bar{\alpha}_s(t) = \alpha_0 + \theta + (\xi_s - \xi_{cg})c\,\dot{\theta}/U_\infty \tag{7a}$$

$$\bar{\alpha}_N(t - \Delta t) = \alpha_0 + \theta - (\xi_{cg} + \xi_s U_\infty/\bar{U})c\,\dot{\theta}/U_\infty \tag{7b}$$

Combining Eqs. (2) and (7) gives

$$N_s(t) = \left(\frac{\rho_\infty U_\infty^2}{2}\right)\left(\frac{\pi d^2}{2}\right)C_{Ns}(t) \tag{8a}$$

$$C_{Ns}(t) = \left(\frac{\partial C_{Ns}}{\partial \alpha_s}\right)\left[\alpha_0 + \theta + (\xi_s - \xi_{cg})\frac{c\,\dot{\theta}}{U_\infty}\right] + \left(\frac{\partial C_{Ns}}{\partial \alpha_N}\right)\left[\alpha_0 + \theta - \left(\xi_{cg} + \frac{\xi_s U_\infty}{\bar{U}}\right)\frac{c\,\dot{\theta}}{U_\infty}\right] \tag{8b}$$

Equation (8b) can be rewritten as

$$C_{Ns}(t) = \left(C_{N\alpha s} + \Delta^i C_{N\alpha s}\right)(\alpha_0 + \theta) + \left[(\xi_s - \xi_{cg})C_{N\alpha s} - (\xi_{cg} + \xi_s U_\infty/\bar{U})\Delta^i C_{N\alpha s}\right] \tag{9}$$

where $C_{N\alpha s} = \partial C_{Ns}/\partial \alpha_s$ and $\Delta^i C_{N\alpha s} = \partial C_{Ns}/\partial \alpha_N$.

For slow oscillations at low frequencies and small amplitudes, Eq. (9) defines the following derivatives:

$$\frac{\partial C_{Ns}}{\partial \theta} = C_{N\dot{\theta}s} = C_{N\alpha s} + \Delta^i C_{N\alpha s} \tag{10}$$

$$\frac{\partial C_{Ns}}{\partial (c\,\dot{\theta}/U_\infty)} = C_{N\dot{\theta}s} = (\xi_s - \xi_{cg})C_{N\alpha s} - \left(\xi_{cg} + \frac{\xi_s U_\infty}{\bar{U}}\right)\Delta^i C_{N\alpha s} \tag{11}$$

Equations (10) and (11) will be used to demonstrate the disproportionately large effect of the separation-induced flare force on the vehicle dynamics in elastic bending oscillations or rigid-body pitch oscillations. For simplicity, let $\xi_{cg} - \xi_N = \xi_s - \xi_{cg}$ (Fig. 6) and $\Delta^i C_{N\alpha s} = C_{N\alpha s}$ in Eqs. (10) and (11). With $\Delta^i C_{N\alpha s} = C_{N\alpha s}$ and $\bar{U}/U_\infty = [C_{AS}/C_{Aa}]^{1/2} = 2$ (Ref. 9, Fig. 6), Eq. (11) gives

$$C_N\dot{\theta}_s = -2\xi_{cg}C_{N\theta s} \tag{12}$$

For the Polaris reentry body (Fig. 4a) the separation-induced undamping was of much larger magnitude than that indicated by Eq. (12). In Fig. 4a, the $C_m(\alpha)$ slopes can represent $C_N(\alpha)$ slopes in Eq. (10) because the dominant (and only statically stabilizing) contribution comes from the flare. At $\alpha > 4$ deg, the slope is the result of the loads generated by the attached flow on the windward half of the flare. That is, the slope would be twice as high in attached flow at $\alpha = 0$. However, in the separated flow region embedding the flare at $|\alpha| < 4$ deg, $C_{N\alpha s}$ would be much less, probably less than for $\alpha > 4$ deg. Figure 4a gives a value for the $C_m(\alpha)$ slope that is eight times larger for $|\alpha| < 4$ deg than for $\alpha > 4$ deg. That is, $C_{N\alpha s}$ would probably be less than one-eight of the value of $\Delta^i C_{N\alpha s}$ for the Polaris reentry body, and Eq. (12) would take the following form:

$$C_N\dot{\theta}_s = -16\,\xi_{cg}C_{N\theta s} \tag{13}$$

which explains the magnitude of the undamping measured at $M = 0.95$ (Fig. 5). The effect of the escape-rocket wake on the Apollo command module (Fig. 2) is similar to this effect of the nose-induced flow separation on the flare of the Polaris reentry body (Fig. 6).

In the case of the Able payload shape (Fig. 1), the accelerated-flow effect[12] adds to the effect of the convective-flow time lag. During the upstroke, the boundary layer forward of flow separation has been experiencing lower adverse pressure gradients than in the static case, which causes a delay of flow separation in addition to that occurring through the convective flow time-lag effect discussed earlier. During the downstroke, the effect is the opposite, also promoting flow separation. That is, the effect is analogous to increasing the convective-flow time lag.

The accelerated flow effect is computed as follows. The pressure gradient of the external flow at the edge of the boundary layer is given by the complete Bernoulli equation

$$-\left(\frac{1}{\rho}\right)\left(\frac{\partial p_e}{\partial x}\right) = \frac{\partial U_e}{\partial t} + U_e\left(\frac{\partial U_e}{\partial x}\right) \tag{14}$$

For constant vehicle velocity, U_e changes only through body pitching or bending,

$$\frac{\partial p_e}{\partial \xi} = -\rho_e U_e\left[\left(\frac{\partial U_e}{\partial \theta}\right)\left(\frac{c\,\dot{\theta}}{U_e}\right) + \frac{\partial U_e}{\partial \xi}\right] = -\rho_e\left[\frac{\partial\left(U_e^2/2\right)}{\partial \theta}\right]\left(\frac{c\,\dot{\theta}}{U_e}\right) - \rho_e\left[\frac{\partial\left(U_e^2/2\right)}{\partial \xi}\right] \tag{15}$$

That is,

$$\frac{\partial Cp}{\partial \xi} = \left(\frac{\partial Cp_e}{\partial \xi}\right)_{\dot{\theta}=0} + \left(\frac{\partial Cp_e}{\partial \theta}\right)\left(\frac{c\,\dot{\theta}}{U_e}\right) \tag{16}$$

Through Prandtl–Meyer expansion, $\partial Cp_e/\partial\theta$ is obtained as

$$\frac{\partial Cp_e}{\partial \theta} = -\left(\frac{2}{\gamma M_\infty^2}\right)\frac{\partial(p_e/p_\infty)}{\partial v} = -2\left(\frac{M_e^2}{M_\infty^2}\right)\left(M_e^2 - 1\right)^{-\frac{1}{2}} \tag{17}$$

Equation (17) gives for $M_e = \sqrt{2}$

$$\frac{\partial Cp_e}{\partial \theta} = \frac{-4}{M_\infty^2} \tag{18}$$

Thus, the body pitching (or bending) motion $c\,\dot{\theta}/U_e > 0$ decreases the pressure gradient $\partial Cp_e/\partial\xi$ and will, therefore, delay boundary-layer separation. That is, the separation will lag behind its static or steady-state position. This lag, added to the convective flow time lag, made the flow separation on the Able payload shroud have a strongly adverse effect on the elastic vehicle dynamics, resulting in the loss of the Able IV payload.

It has been demonstrated that flow separation has opposite effects on static and dynamic stability, for example, increasing static stability but decreasing dynamic stability, as in the case of the Polaris reentry body. Whereas static stability is important for the reentry body, in the case of the elastic launch vehicle aerodynamics, the aerodynamic stiffness (corresponding to the static stability for the reentry body) is usually negligible compared to the structural stiffness. Thus, the only significant effect of the flow separation is to decrease the launch vehicle damping. Flow separation should, therefore, be avoided to the largest extent possible.

Saturn–Apollo Launch Vehicles

The difference in Fig. 2 between the measured static loads and those expected in attached flow indicates that it is very important to account for the effect of separated flow, especially when considering the corresponding dynamic loads, as was demonstrated earlier for the rigid-body dynamics of the Polaris reentry body (Fig. 5). Actually, the separation-induced loads are of larger magnitude than what Fig. 2 indicates, as is illustrated in Fig. 7a for the effect of the escape-rocket wake on the static force measured on the Apollo command module.[7,8] The load component $C_{N\alpha s}$, dependent on the local angle of attack, is less than that for attached flow because of the velocity deficit in the escape-rocket wake. The difference $\Delta^i C_{N\alpha s} = C_{N\alpha \text{total}} - C_{N\alpha s}$ is the load component dependent on the effective angle of attack of the escape rocket. Figure 7b shows how $\Delta^i C_{N\alpha s}$ is composed of the components $\Delta^i C_{N\beta s}$ and $\Delta^i C_{N\theta s}$ generated by the escape-rocket perturbation in translation and rotation, respectively. The negative force derivatives $C_{N\alpha s}$ and $\Delta^i C_{N\alpha s}$ for the load on the cone-cylinder shoulder are composed in a similar manner. Because these separation-induced loads not only were of large magnitude but also were associated with large convective-flow time-lag effects, they dominated the elastic vehicle dynamics[7,8] (Fig. 8).

The separation-induced normal force derivative $(C_{N\alpha s})/dx$, generated on the Apollo command module by the local angle of attack α_s, was estimated by accounting for the velocity deficit in the wake, using the axial-force ratio[7,8] $(C_{A0})_s/(C_{A0})_a$ (Fig. 7). The remainder of the measured normal force derivative, $\Delta^i C_{n\alpha s} = (C_{n\alpha})_{\text{total}} - C_{n\alpha s}$, was assumed to be produced by the wake-directing effect of the escape rocket and, therefore, subject to convective flow time-lag effects. A similar partitioning was performed for the force generated on the Apollo–Saturn shoulder. When the convective flow time lag was accounted for when applying the loads generated by the escape-rocket wake, the aerodynamic damping in percent of critical could be computed for the first two bending modes of the Saturn I–Apollo launch vehicle (Fig. 8). It can be seen that the predicted damping[7,8] is in satisfactory agreement with measurements.[13] The results shown for attached-flow treatment represent the classic quasi-steady prediction, in which the convective-flow time-lag effect is not considered.

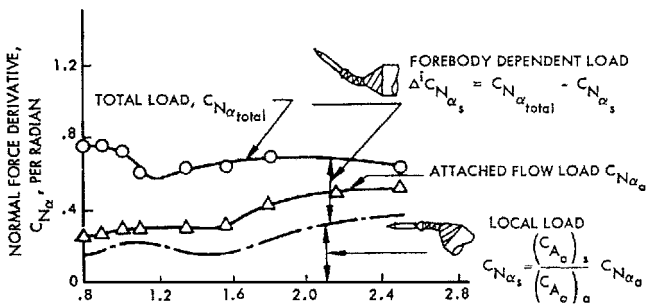

a) Forebody-dependent and local loads

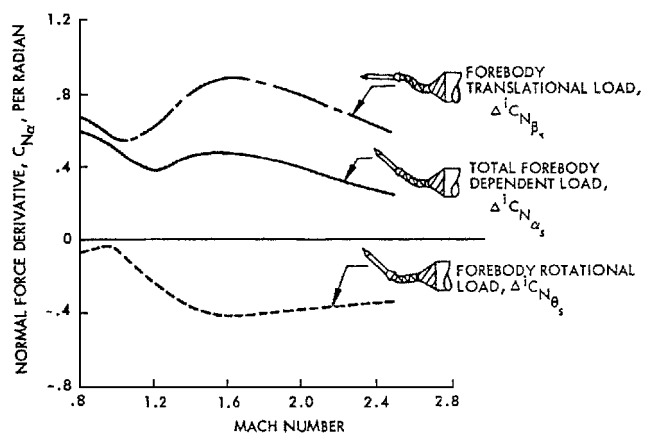

b) Forebody-dependent translational and rotational loads

Fig. 7 Loads on the Apollo command module in the wake from the escape rocket.[8]

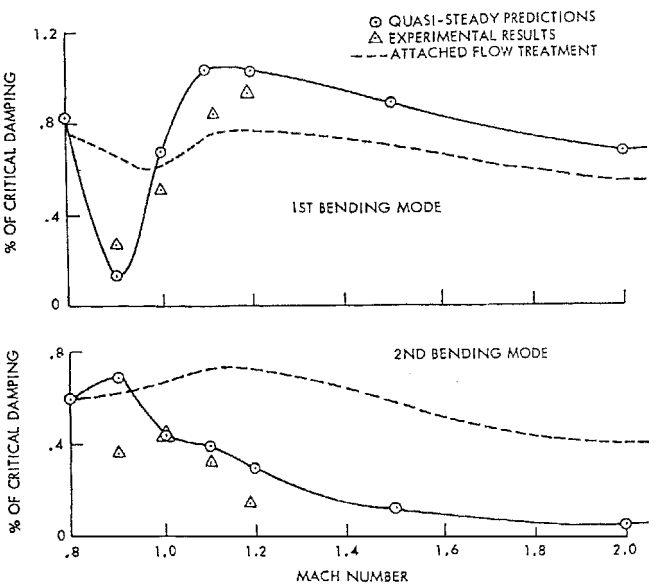

Fig. 8 Aerodynamic damping at $\alpha = 0$ of the first and second bending modes of the Saturn I–Apollo launch vehicle.[7]

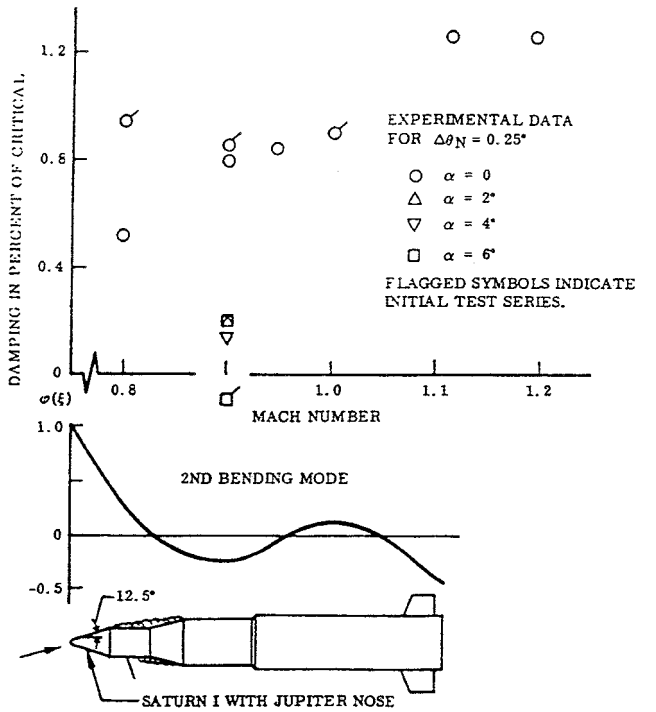

Fig. 9 Aerodynamic damping at $\alpha = 0$ of an 8% elastic model of the Saturn I, Block II launch vehicle with a Jupiter nose.[14]

Cone–Cylinder Configurations

The linear aerodynamic analysis,[7,8] which by accounting for convective-flow time-lag effects successfully could predict the measured damping for the Saturn–Apollo launch vehicle[13] (Fig. 8), could not predict the experimental data trend for the second bending mode of the Saturn I, Block II launch vehicle with a Jupiter payload shroud[14] (Fig. 9). When the angle of attack was increased to 6 deg, a 1% drop of the aerodynamic damping occurred at $M = 0.9$, which lead to a complete loss of aerodynamic damping. The flow phenomenon responsible for this result was first discovered by Robertson,[15] Robertson and Chevalier,[16] and Chevalier and Robertson[17] (Fig. 10). At high subsonic speeds, a terminal shock appears downstream of the cone–cylinder shoulder and causes local boundary-layer separation. When the angle of attack is increased above a critical value, $2 < \alpha < 4$ deg for $\theta_c = 20$ deg, the leeward side flow separation jumps forward to the cone–cylinder shoulder,

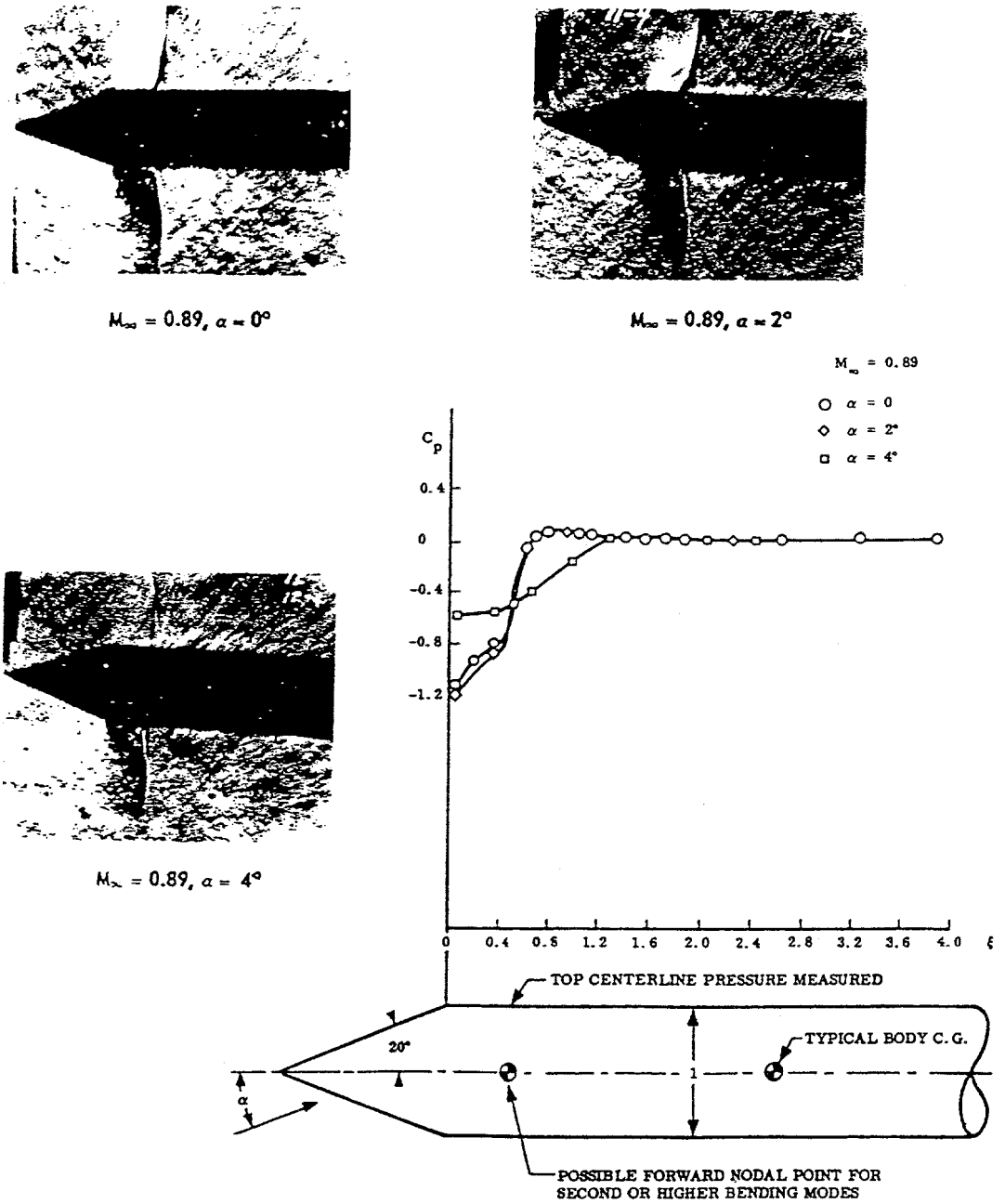

Fig. 10 Aerodynamic characteristics at $M = 0.89$ of a 20-deg cone–cylinder body.[16]

which causes a large, discontinuous load change. The jump to complete leeward side flow separation occurs at higher angle of attack the smaller the semicone angle θ_c is.[16] The use of a porous surface[18] (Fig. 11) would have eliminated the sudden separation phenomenon by changing the single shock with associated local flow separation (Figs. 10 and 11) to a series of shocks with their more limited, local flow separations. However, for aerospace launch vehicles, a more practical solution is to use the biconic nose geometry discussed later.

At $M = 0.95$ local shock-induced flow separation occurs aft of the 20-deg cone–cylinder shoulder[16] (Fig. 12). At nonzero angle of attack, the leeward side shock moves forward of the windward side shock, generating a force couple, which is of much smaller magnitude than that resulting through the change from shock-induced to nose-induced flow separation (Fig. 10). The linear analysis required to predict the aeroelastic effect of the shock-induced flow separation (Fig. 12), extending the Saturn–Apollo analysis[7,8] to include the accelerated flow effect, is described in Ref. 12. For the Saturn–Apollo configurations considered in Refs. 7 and 8, the accelerated-flow effect is negligibly small compared to the effect of convective-flow time lag in the crossflow influence on the boundary-layer growth. However, the accelerated-flow effect plays a dominant role in the nonlinear analysis required to determine the limit-cycle amplitude of the bending oscillation resulting in the case of the sudden change from shock-induced to nose-induced flow separation (Figs. 12 and 10, respectively).

The terminal shock and the associated boundary-layer separation moves forward on the leeward side with increasing angle of attack at subsonic Mach numbers. When the shock on the leeward side approaches the cone–cylinder shoulder, with associated highly adverse pressure gradients, the local, shock-induced flow separation changes to the global, nose-induced separation type, which results in the pressure distribution shown for $\alpha = 4$ deg in Fig. 10 for the leeward side of a 20-deg cone–cylinder configuration. This sudden change from shock-induced to nose-induced flow separation generates one undamping component that is independent of the oscillation amplitude and results in a limit-cycle type of oscillation. That is, the oscillation amplitude will increase until the separation-induced undamping is balanced by the available damping, which usually is limited to the structural damping in a conservative analysis.

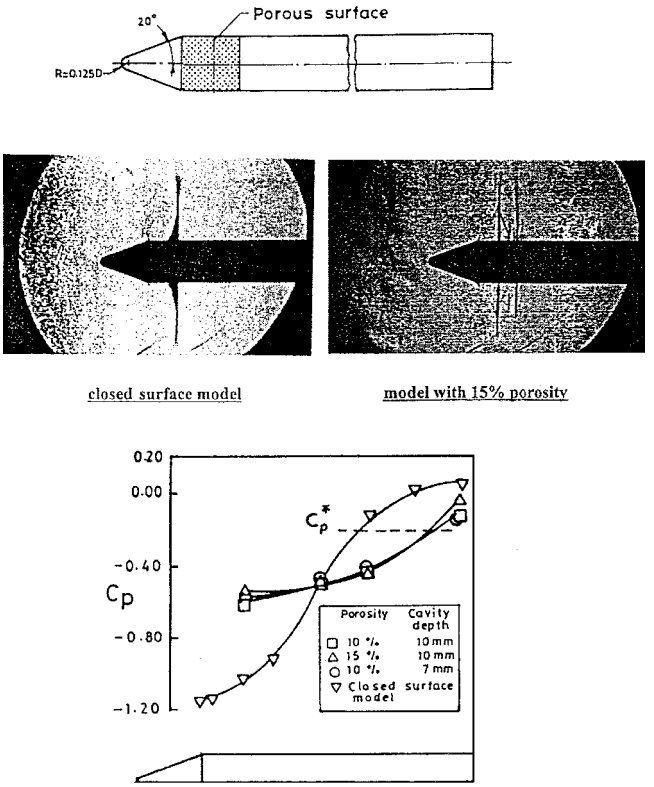

Fig. 11 Effect of porous surface on the aerodynamic characteristics of a 20-deg cone-cylinder at $M = 0.90$ and $\alpha = 0$ (Ref. 18).

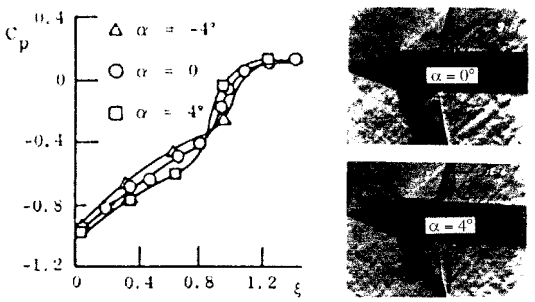

Fig. 12 Aerodynamic characteristics at $M = 0.95$ of a 20-deg cone-cylinder body.[16]

To ensure the structural integrity of the launch vehicle, it is required in the case of the linear analysis[2,3,7] that the magnitude of the aerodynamic undamping does not exceed the structural damping. In the nonlinear case, the requirement is that the amplitude of the bending oscillations does not exceed the limiting value for preservation of the structural integrity of the launch vehicle. For the structural characteristics of the Saturn V launch vehicle,[19,20] the initial growth rates $\partial M_{\text{static}}/\delta\alpha$ and $\partial M_{\text{dyn}}/\partial(\Delta\theta_N)$ of the static and dynamic bending moments for the first bending mode were as shown in Fig. 13 (Ref. 21). Figure 13 demonstrates that bending oscillations reaching 1-deg amplitute at the nose ($\Delta\theta_N = 1$ deg) produced the same bending moment over the first 40 m of the vehicle as a static angle of attack of 10 deg ($\alpha = 10$ deg). The nonlinear analysis required to determine the limit-cycle amplitude $\Delta\theta_N$ is described in Ref. 12.

Commercial Aerospace Launch Vehicles

The Seasat-A was an experimental satellite designed to monitor the world's oceans on a near-real-time basis. It was lofted atop an Atlas–Agena booster. The original 84-in.-diam Seasat-A shroud just covered the payload and was faired to the smaller diameter Agena upper stage with a conical frustum (Fig. 14a). The Agena in turn was faired to the larger diameter Atlas first stage via another conic frustum. The resulting hammerhead configuration violated one important design criterion specified by NASA.[22] The $164/84 = 1.95$ gap between the base of the hammerhead shroud and the following Atlas–Agena interstage flare should have been at least 2.8. The flow phenomenon endangering the structural integrity was the sudden leeside merging (at a certain α) of the hammerhead wake and the flare-induced flow separation forward of the Atlas–Agena interstage frustum[23] (Fig. 14b), which results in a sudden discontinuous load change on the cylinder and flare aft of the hammerhead.

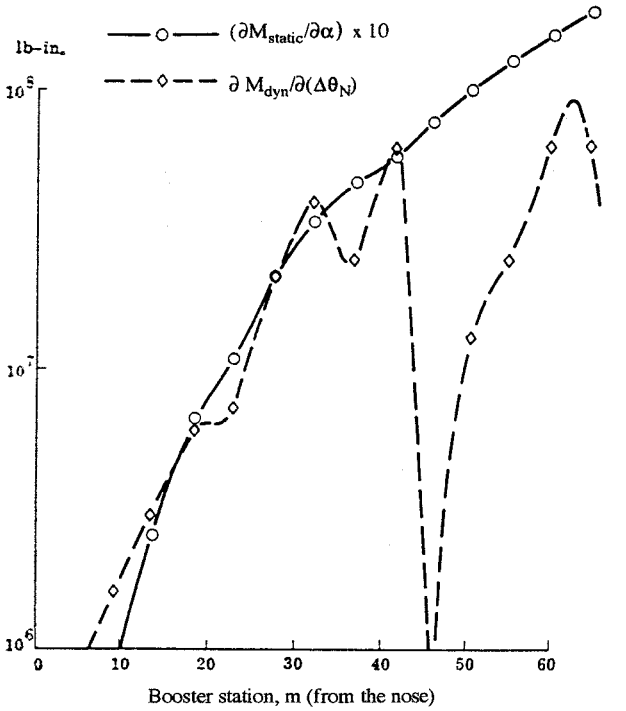

Fig. 13 Comparison of the initial growth of dynamic and static bending moments on Saturn V at maximum dynamic pressure, $M = 1.6$, $\alpha = 0$, and $\Delta\theta_N = 0$ (first bending mode).[21]

A nonlinear aeroelastic analysis[23] showed that it was possible that the Seasat-A, as originally designed, could experience dynamic aeroelastic instability. Consequently, two alternative shroud modifications were proposed: 1) lengthening the Agena section (Fig. 14a) to achieve the required $2.8d$ separation between the payload and the Atlas–Agena interstage flare and redesigning the hammerhead payload shroud to meet the NASA criterion[22] and 2) elimination of the hammerhead geometry altogether. The first solution increased the bending loads at the Atlas–Agena interstage to unacceptable levels. Therefore, it was decided to eliminate the hammerhead by enclosing both the payload and the Agena upper stage in a cylindrical fairing that had a diameter equal to the booster diameter (Fig. 14c). In addition, the redesigned shroud featured a biconic nose that has been shown to eliminate the sudden flow separation occurring at high subsonic speeds on a regular cone–cylinder shoulder[12,24] (Fig. 15). Thus, the new shroud eliminated all separation-induced unsteady flow phenomena that could adversely affect the aeroelastic stability. It had the additional advantage of reducing the drag by eliminating the base and frustum drag on the Atlas–Agena interstage. These drag reductions more than offset the additional pressure drag on the larger diameter nose and the added skin-friction drag on the larger diameter cylinder.

A hammerhead launch vehicle geometry[25] (Fig. 16a), tested using the Cole et al. partial mode technique[26] (Fig. 16b), gave the results shown in Fig. 16c and demonstrated that the parameter L_N/d_N played an important role. Apparently, the character of the flow separation changes dramatically when this parameter is decreased to $L_N/d_N = 0.3$ (and below), which produces a sudden increase of the buffet response at transonic speeds, $0.8 < M < 1.0$. Data for similar hammerhead configurations indicate that the pressure in the base-flow region remains constant[27] (Fig. 17a). Just ahead of the base a shock-induced pressure rise occurs, which has a dramatic effect on the pressure distribution at $\alpha = 4$ deg and $M = 0.88$ (Fig. 17b).

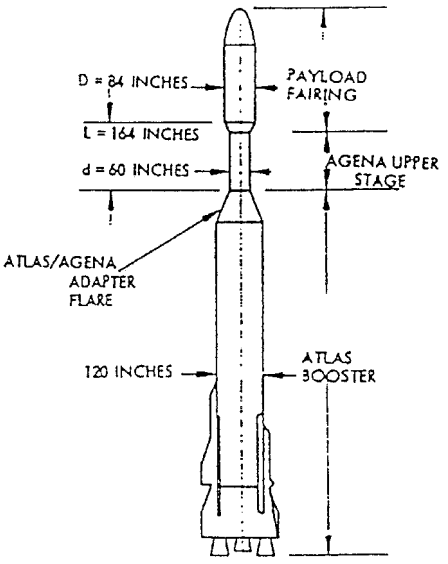

a) Launch vehicle geometry

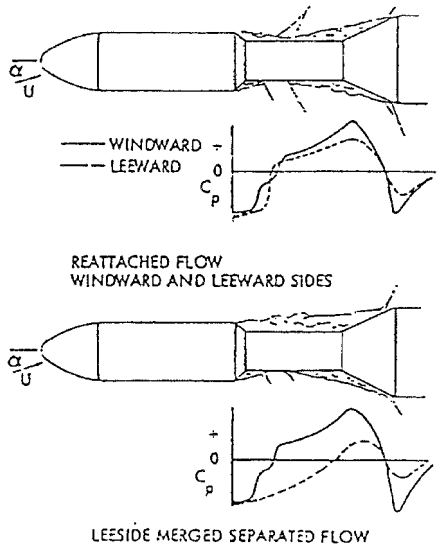

b) Sudden change of flow structure

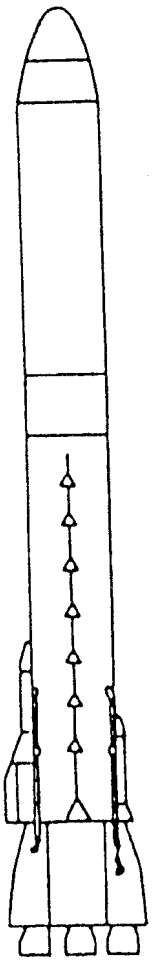

c) Revised launch vehicle geometry

Fig. 14 Seasat-A launch vehicle.[23]

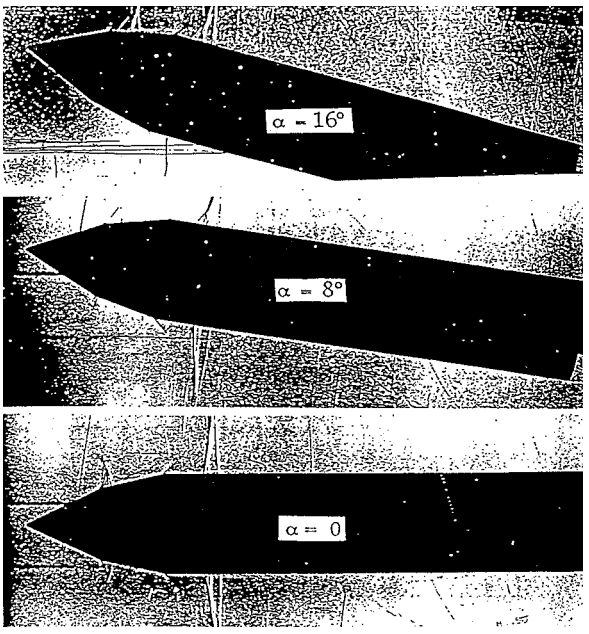

Fig. 15 Flow at $M = 0.9$ over the Saturn IB SA-203 launch vehicle with a biconic payload shroud.[24]

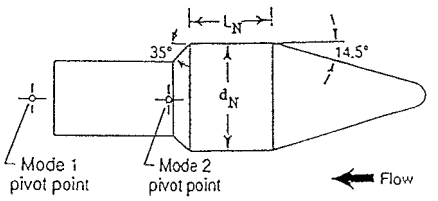

a) Hammerhead geometry

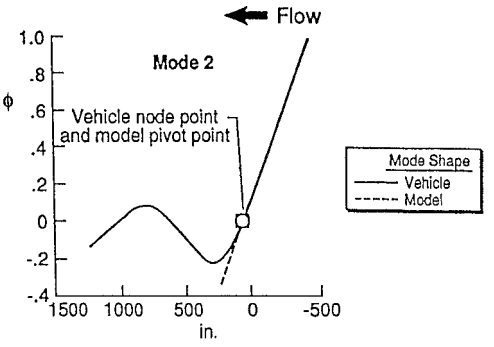

b) Normalized mode shape for second bending mode

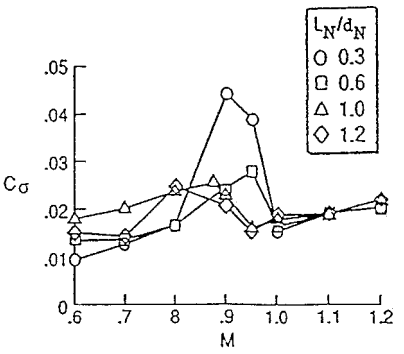

c) Effect of L_N/d_N on buffet response for the second bending mode

Fig. 16 Test of hammerhead launch vehicle.[25,26]

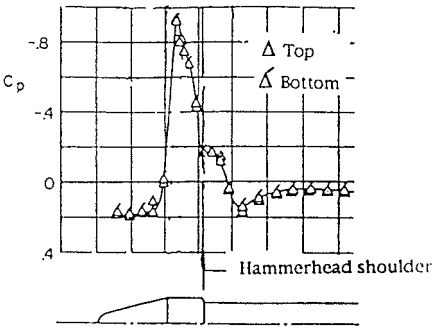

a) $\alpha = 0$ deg

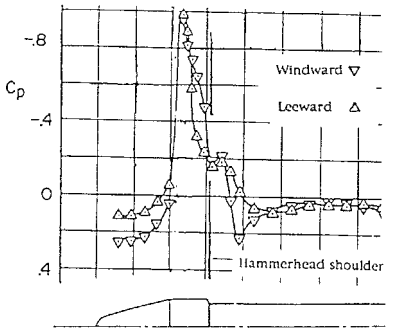

b) $\alpha = 4$ deg

Fig. 17 Measured static pressure distribution on a candidate hammerhead geometry at $M = 0.88$ and $\alpha = 0$ (Ref. 25).

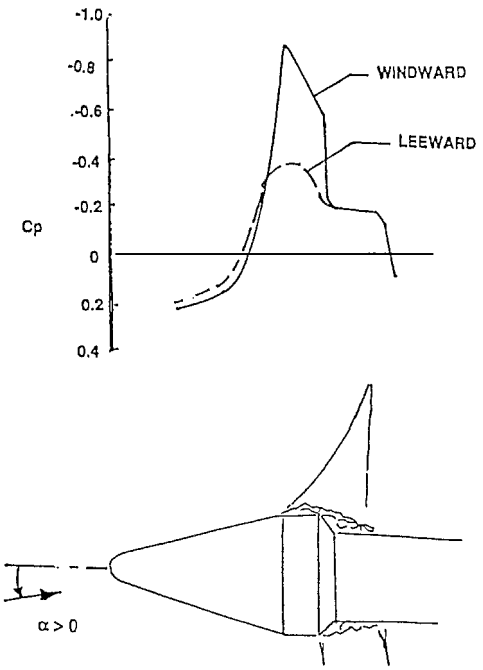

Fig. 18 Conceptual pressure distribution caused by sudden leeside flow separation on 0.3-caliber hammerhead cylinder at M = 0.89 (Ref. 28).

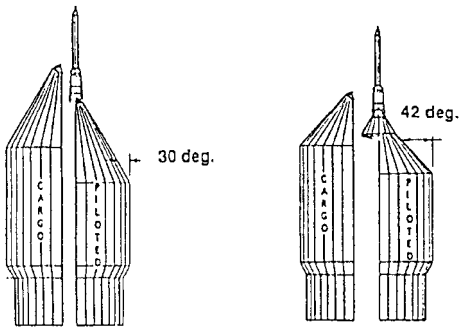

Fig. 19 HLLV noses.[28]

When the cylinder is very short (0.3 calibers or less in the present case) any forward movement of the leeside shock will produce an extremely large adverse pressure gradient, which interacts with the low expansion pressures at the cone–cylinder shoulder and generates a negative shoulder load of large magnitude forward of the base[28] (Fig. 18). Because the forward node of the second bending mode is located aft of the base (Fig. 16a), the separation-induced, discontinuous, negative, statically stabilizing force will be dynamically destabilizing or undamping[7,8] and result in the large buffet loads shown in Fig. 16c for $L_N/d_N = 0.3$.

Heavy lift launch vehicle (HLLV) designs have used very steep nose-cone angles to minimize weight[28] (Fig. 19). These configurations violate the NASA guidelines for aeroelastic stability,[22] which recommend a nose-cone angle of 15 deg or less to avoid the transonic nose-induced flow separation discussed earlier. Figure 20 presents a typical pressure distribution for nose-induced flow separation on the Saturn I–Apollo launch vehicle with the escape rocket removed.[7,29] Figure 20 shows the potential for aerodynamic undamping of a bending mode with the forward nodal point ahead of the flare. The fluid mechanics are basically similar to those generating the measured undamping on the Polaris reentry body[9,10] (Figs. 3–5).

Early results for a biconic hammerhead geometry[30] (Fig. 21) showed the danger potential of the hammerhead-wake-reattachment phenomenon to be modest, for the particular mode shape tested. It generated negative damping or undamping of modest magnitudes at $M = 0.95$ and 1.0 and resulted in $\zeta_a + \zeta_s + \zeta_0 < \zeta_0$. However, the large positive aerodynamic damping measured at $M = 0.9$, 0.6% of

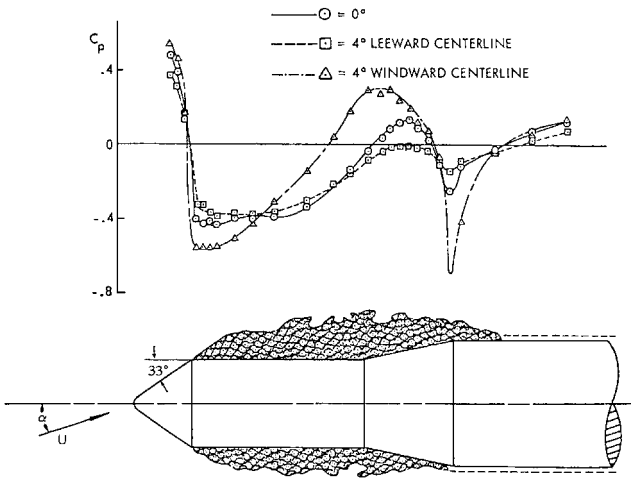

Fig. 20 Saturn forebody pressure distribution at M = 0.9 with escape rocket removed.[7]

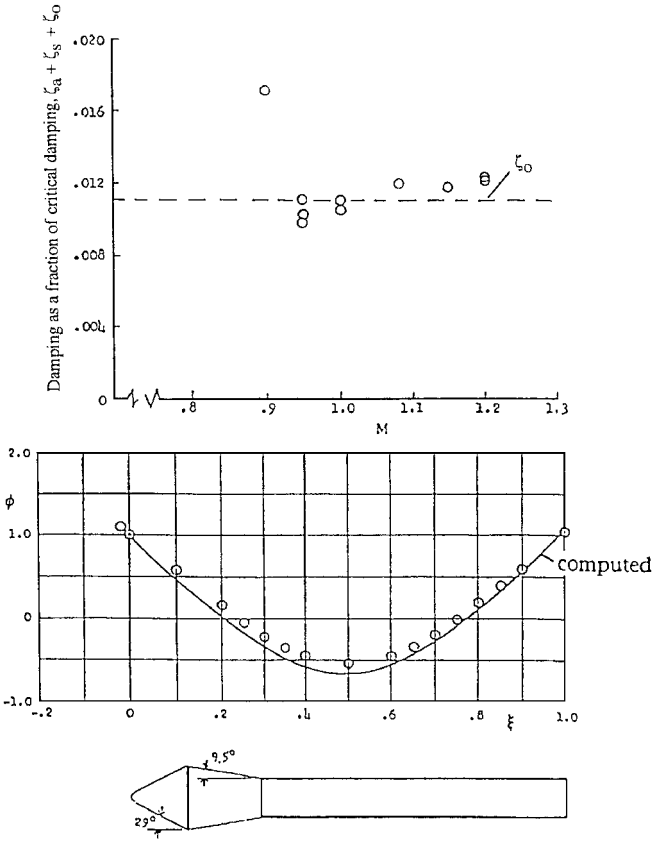

Fig. 21 Experimental damping characteristics as a fraction of critical damping for the first bending mode of a biconic hammerhead configuration.[30]

critical, showed that the wake reattachment on the 9.5-deg boattail generated large aeroelastic damping effects. In Fig. 22, the flow has been added to illustrate the flow physics causing the different aeroelastic effects.[31] At $M = 0.95$ and 1.0, the wake reattaches rather early on the windward side of the boattail and produces a negative normal force component. The generative process is very similar to that for the nose-induced flow separation at $M = 0.9$ in Fig. 20. The negative normal force generates a statically stabilizing moment at $M = 0.95$ and 1.0 for the original mode shape (open symbol) in Fig. 22, which through the convective flow time lag discussed earlier produces a dynamically destabilizing effect and results in the measured negative aerodynamic damping. At $M = 0.9$, however, the hammerhead wake does not reattach until downstream of the boattail–cylinder juncture, judging by unsteady pressure measurements[32] (Fig. 23). Consequently, the negative normal force is in this case located aft of

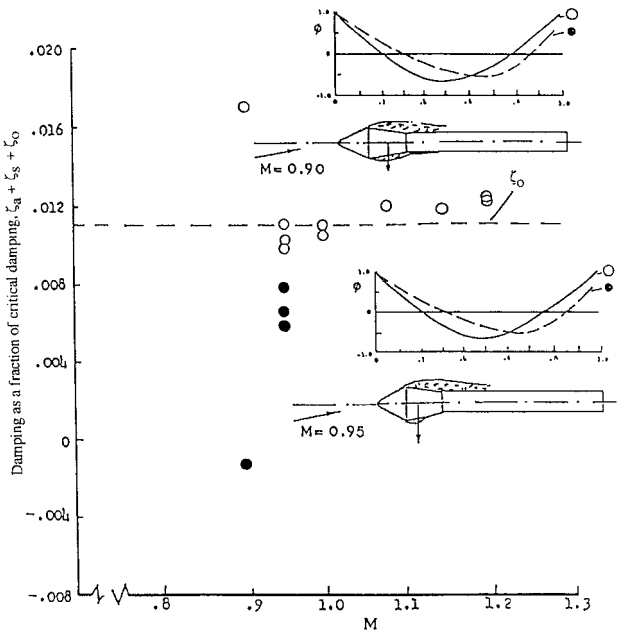

Fig. 22 Effects on damping of a slight change of mode shape for a biconic hammerhead geometry.[30,31]

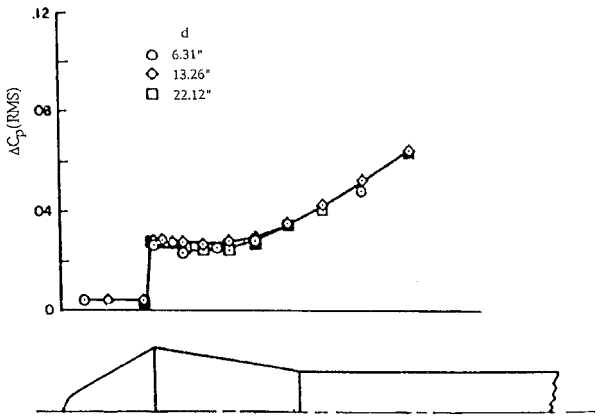

Fig. 23 Fluctuating pressure distribution on cylinder with biconic hammerhead.[32]

the forward nodal point in Fig. 22 and generates a statically destabilizing/dynamically stabilizing moment that results in the measured large positive damping (0.6% of critical).

If one considers the effect of a more realistic aft booster geometry,[31] the mode shape could change as shown (solid symbol in Fig. 22), causing the forward nodal point to be located aft of the negative normal force also at $M = 0.9$. If the apparent mass and frequency of the bending mode were to remain the same, the analysis in Ref. 11 predicts the aerodynamic damping to change as indicated by the solid data points in Fig. 22. That is, for this mode shape roughly -1.0% of critical aerodynamic undamping would be measured rather than $+0.6\%$ aerodynamic damping. For the widely used liquid-propellant rockets, the structural damping is usually only a fraction of 1%.

In a recent analysis of the aeroelastic vehicle dynamics of a proposed Delta II 7920-10L launch vehicle,[33] the original two candidate payload–shroud geometries (Fig. 24) were subject to many of the adverse separated-flow dynamics discussed earlier. Both shroud geometries could be expected to experience nose-induced flow separation at high subsonic speeds. Thus, the experimental results for the Polaris reentry body[9,34] (Figs. 3–5) and the Saturn–Apollo geometry (Fig. 20) can be used to illustrate the highly nonlinear, discontinuous flow separation characteristics expected for the Delta shroud geometries (Fig. 24). A discontinuous change from retarded shock-induced to nose-induced leeside flow separation occurs at

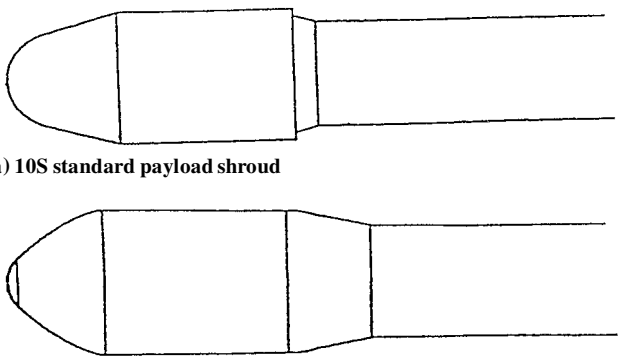

a) 10S standard payload shroud

b) 10L composite payload shroud

Fig. 24 Delta payload shroud configurations.[33]

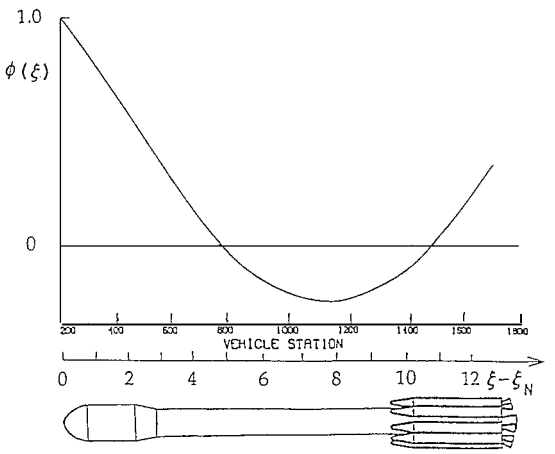

a) First bending mode

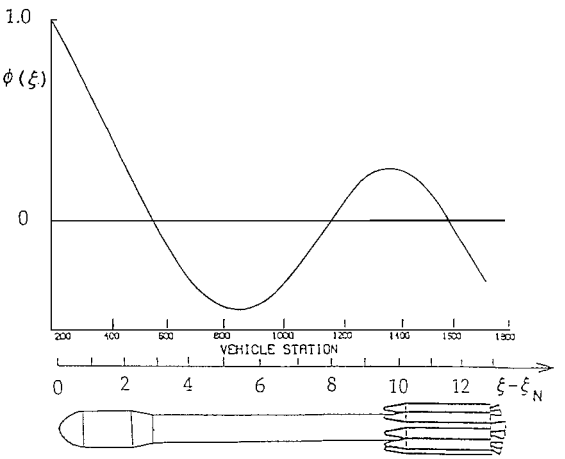

b) Second bending mode

Fig. 25 Bending mode shapes of proposed Delta II 7920 launch vehicle with 10L payload shroud.[33]

$|\alpha| = \alpha_{crit} > 0$, similar to the change occurring on the cone–cylinder in Fig. 10, where $2 < \alpha_{crit} < 4$ deg.

An analysis was performed of the elastic vehicle dynamics of the 10L composite payload shroud (Fig. 24b) for single-degree-of-freedom oscillations in the first and second bending modes[33] (Fig. 25). The key information needed in such an analysis is a description of the loads generated by the occurring flow separation. These loads are determined as the difference between loads measured in wind-tunnel tests and the theoretical loading existing in inviscid flow. In earlier analyses of cone–cylinder geometries,[12,35] the inviscid loads were determined by a shock-expansion method.[36] In the present case, they were obtained by solving the Euler equations[37,38] (Fig. 26). The force couple defined by the difference from the experimental results is generated by the flow separation.

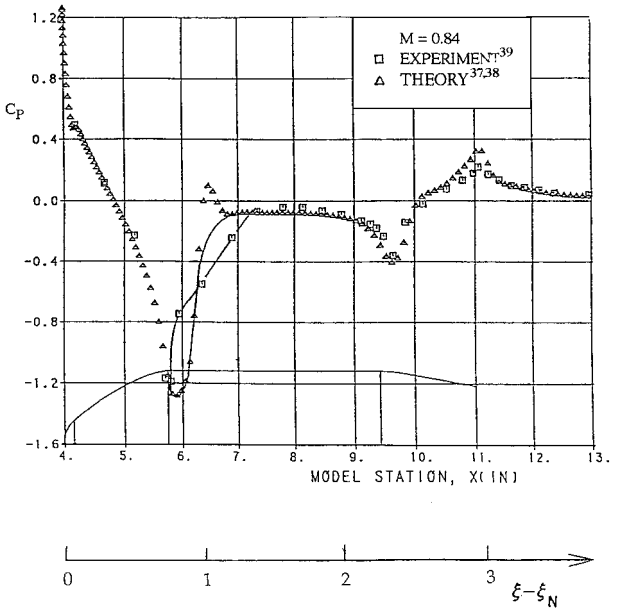

Fig. 26 Pressure distribution over proposed Delta II 7920-10L payload shroud at α = 3 deg and M = 0.80.

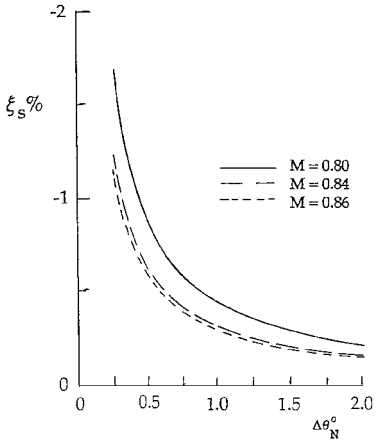

Fig. 27 Separation-induced undamping in percent of critical damping as a function of amplitude $\Delta\theta_N$ at the nose tip for the first bending mode of proposed Delta II 7920 launch vehicle with the 10L payload shroud.[33]

It is similar to that in Fig. 10 for the 20-deg cone–cylinder geometry. Using the developed computational means[33] gave the dynamic results in Fig. 27, which show the aerodynamic undamping in percent of critical for the first bending mode (Fig. 25a). The oscillation amplitude $\Delta\theta_N = 0.28$ deg, resulting at $M = 0.80$ for the available 1.5% structural damping, was well within the structural capability.

Conclusions

A review of past tests and analyses of the elastic vehicle dynamics of aerospace launch vehicles reveals that subtle changes of the payload shroud geometry can cause dramatic changes of the separated flow phenomena, which makes it practically impossible to define geometric guidelines for the design of the payload shroud that will guarantee the absence of any of the undesirable separated flow phenomena. The only realistic approach is to test the geometry selected for spacial or structural reasons to determine if any flow separation category is present that has been shown in the past to be capable of generating a problem for the elastic vehicle dynamics. It is concluded that the following efforts would offer the best opportunity for the launch vehicle designer to avoid the unsteady separated flow phenomena that in the past have been shown to have the capability to endanger the structural integrity of the launch vehicle.

1) Adding flow visualization to the experiments planned for the determination of the static loads can reveal whether any of the discussed adverse unsteady flow separation phenomena could occur on the selected launch vehicle design. If this is considered to be a definite possibility, a modest extension of the static tests can provide the database needed for the computation of the elastic vehicle dynamics with the accuracy needed for preliminary design through the use of developed computational means that account for the effects of flow acceleration and convective flow time lag.

2) Usually only a conservative analysis of the elastic vehicle response in the first and second low-frequency bending modes is needed to assure the structural integrity of the launch vehicle.

3) If the conservative analysis indicates that the launch vehicle could possibly experience dynamic aeroelastic instability, two courses of action are available. First, redesign of the launch vehicle geometry, as exemplified by the case of the Seasat-A launch vehicle (Fig. 14). Second, if a needed substantial redesign of the launch vehicle is not an available option, a more accurate aeroelastic analysis will be needed before it can be determined if a somewhat less extensive redesign will have the required effect. Because the outlined analysis pinpoints the dynamic flow phenomenon or flow phenomena that can be endangering the structural integrity of the launch vehicle, it provides the needed guidelines for satisfactory redesign. The experience so far has been that only a conservative first-order analysis was needed.

Acknowledgment

The author is indebted to J. Peter Reding, with whom he performed numerous analyses in the past under contract to NASA and NAVY DOD. As is evidenced by the references, the summarized results of these analyses form a substantial part of this review paper.

References

[1]Coe, C. F., "Steady and Fluctuating Pressures at Transonic Speeds on Two Space Vehicle Payload Shapes," NASA TM X503, March 1961.

[2]Ericsson, L. E., Woods, P., and Chavez, J. N., "A Mechanism for Self-Excited Oscillations on 'Hammerhead' and Other Blunt-Nosed Missiles," *Proceedings of the 6th Symposium on Ballistic Missile and Aerospace Technology*, edited by C. T. Morrow, L. D. Ely, and M. R. Smith, Vol. 4, Academic Press, New York, 1961, pp. 69–88.

[3]Woods, P., and Ericsson, L. E., "Aeroelastic Considerations in a Slender Blunt-Nose, Multistage Rocket," *Aerospace Engineering*, Vol. 21, No. 5, 1962, pp. 42–51.

[4]Graham, F. J., and Butler, C. B., "Static Pressure Distribution on a 0.07 Scale Aerodynamic Model of the Atlas-Able IV at Free-Stream Mach Numbers from 0.50 to 1.60," Arnold Engieering Development Center, TN-60-128, Arnold AFB, TN, July 1960.

[5]Kistler, A. L., and Chen, W. S., "The Fluctuating Pressure Field in a Supersonic Turbulent Boundary Layer," Jet Propulsion Lab., TR 32-277, California Inst. of Technology, Pasadena, CA, Aug. 1962.

[6]Speaker, W. V., and Ailman, C. M., "Static and Fluctuating Pressures in Regions of Separated Flow," AIAA Paper 66-456, Jan. 1966.

[7]Ericsson, L. E., and Reding, J. P., "Analysis of Flow Separation Effects on the Dynamics of a Large Space Booster," *Journal of Spacecraft and Rockets*, Vol. 2, No. 4, 1965, pp. 481–490.

[8]Ericsson, L. E., and Reding, J. P., "Report on Saturn I—Apollo Unsteady Aerodynamics," NASA CR-53375, Feb. 1964.

[9]Ericsson, L. E., "Separated Flow Effects on the Static and Dynamic Stability of Blunt Nosed Cylinder Flare Bodies," NASA CR-76919, Dec. 1965.

[10]Ericsson, L. E., "Unsteady Aerodynamics of Separatiing and Reattaching Flow on Bodies of Revolution," *Recent Research on Unsteady Boundary Layers*, edited by A. E. Eichelbrenner, Vol. 1, IUTAM Symposium, Laval Univ., Quebec, PQ, Canada, 1971, pp. 481–512.

[11]Ericsson, L. E., and Reding, J. P., "Fluid Dynamics of Unsteady Separated Flow. Part I. Bodies of Revolution," *Progress in Aerospace Sciences*, Vol. 23, No. 1, 1986, pp. 1–84.

[12]Ericsson, L. E., "Aeroelastic Instability Caused by Slender Payloads," *Journal of Spacecraft and Rockets*, Vol. 4, No. 1, 1967, pp. 65–73.

[13]Rainey, G., "Progress on the Launch Vehicle Buffeting Problem," *Journal of Spacecraft and Rockets*, Vol. 2, No. 2, 1965, pp. 289–299.

[14]Hanson, P. W., and Dogget, R. V., Jr., "Aerodynamic Damping and Buffet Response of an Aeroelastic Model of the Saturn I—Block II Launch Vehicle," NASA TND-2713, March 1965.

[15]Robertson, J. E., "Unsteady Pressure Phenomena for Basic Missile Shapes at Transonic Speeds," AIAA Paper 64-3, Jan. 1964.

[16]Robertson, J. E., and Chevalier, H. L., "Characteristics of Steady-State Pressures on the Cylindrical Portion of Cone-Cylinder Bodies at Transonic Speeds," Arnold Engineering Development Center, Rept. TDR-63-104, Arnold AFB, TN, Aug. 1963.

[17]Chevalier, H. L., and Robertson, J. E., "Pressure Fluctuations Resulting from Alternating Flow Separation and Attachment at Transonic Speeds,"

Arnold Engineering Development Center, Rept. TDR 63-204, Arnold AFB, TN, Nov. 1963.

[18]Kumaraj, V., and Stanewsky, E., "Suppression of Shock Wave Oscillations on a Blunt Cone-Cylinder," AIAA Paper 97-0269, Jan. 1997.

[19]Riley, G. F., "AS-507 Structural Damping Characteristics," The Boeing Co., Doc. D5-15541, Vol. 2, Contract NAS 8-5608, Seattle, WA, Aug. 1969.

[20]Ivey, W., and Sims, J., "Vibration Analysis of the Saturn V Operational Vehicle," NASA Rept. R-P&VE-SLA-64-11, April 1964.

[21]Ericsson, L. E., Reding, J. P., and Guenther, R. A., "Relative Magnitudes of Stresses Caused by Static and Dynamic Launch Vehicle Loads," *Journal of Spacecraft and Rockets*, Vol. 10, No. 4, 1973, p. 276.

[22]Cole, S. R., and Henning, T. L., "NASA Space Vehicle Design Criteria, Volume II: Structures, Part B: Loads and Structural Dynamics, Chapter 3: Launch and Exit, Section I: Buffeting," NASA SP-8001, May 1964, rev. Nov. 1970.

[23]Reding, J. P., and Ericsson, L. E., "Effect of Aeroelastic Considerations on Seasat-A Payload Shroud Design," *Journal of Spacecraft and Rockets*, Vol. 18, No. 3, 1981, pp. 241–247.

[24]Ericsson, L. E., French, N. F., and Guenther, R. A., "The Aeroelastic Characteristics of the Saturn IB Launch Vehicle with Biconic Paypoad Shroud," Lockheed Missiles and Space Co., Rept. M-37-67-1, Contract NAS 8-11238, Sunnyvale, CA, July 1967.

[25]Cole, S. R., and Henning, T. L., "Dynamic Response of a Hammer-Head Launch Vehicle Wind-Tunnel Model," *Journal of Spacecraft and Rockets*, Vol. 29, No. 3, 1992, pp. 379–385.

[26]Cole, H., Jr., Robinson, R., and Gambucci, B., "Buffeting Response of the Apollo Partial Mode Model at Subsonic and Supersonic Mach Numbers," NASA TN-D2689, Feb. 1965.

[27]Coe, C. F., and Nute, J. B., "Steady and Fluctuating Pressures at Transonic Speeds on Hammerhead Launch Vehicles," NASA TMX-778, Dec. 1978.

[28]Reding, J. P., and Ericsson, L. E., "Hammerhead and Nose–Cylinder–Flare Aeroelastic Stability Revisited," *Journal of Spacecraft and Rockets*, Vol. 32, No. 1, 1995, pp. 55–59.

[29]Reding, J. P., and Ericsson, L. E., "Static Loads on the Saturn I—Apollo Launch Vehicle," Lockheed Missiles and Space Co., Rept. LMSC-803185, Sunnyvale, CA, Aug. 1963.

[30]Hanson, P. W., and Dogget, R. V., Jr., "Wind-Tunnel Measurements of Aerodynamic Damping Derivatives of a Launch Vehicle Vibrating in Free-Free Bending Modes at Mach Numbers from 0.70 to 2.87 and Comparison with Theory," NASA TND-1391, Oct. 1962.

[31]Ericsson, L. E., "Hammerhead Wake Effects on Elastic Vehicle Dynamics," *Journal of Spacecraft and Rockets*, Vol. 32, No. 1, 1995, pp. 55–59.

[32]Coe, C. F., "The Effect of Model Scale on Rigid-Body UnsteadyPressures Associated with Buffeting," *Symposium on Aeroelastic and Dynamic Modeling Technology*, Pt. 2, Air Force Flight Dynamics Lab., Dayton, OH, 1963, pp. 63–85 (RTD-TDR-63-4197).

[33]Ericsson, L. E., and Pavish, D., "Aeroelastic Vehicle Dynamics of a Proposed Delta II 7920-10L Launch Vehicle," *Journal of Spacecraft and Rockets*, Vol. 37, No. 1, 2000, pp. 28–38.

[34]Ericsson, L. E., and Reding, J. P., "Dynamics of Separated Flow," NASA CR-76912, Dec. 1965.

[35]Ericsson, L. E., "Loads Induced by Terminal-Shock–Boundary-Layer Interaction on Cone–Cylinder Bodies," *Journal of Spacecraft and Rockets*, Vol. 7, No. 9, 1970, pp. 1106–1112.

[36]Syvertson, C. A., and Dennis, D. H., "A Second-Order Shock-Expansion Method Applicable to Bodies of Revolution Near Zero Lift," NACA Rept. 1328, 1957.

[37]Jameson, A., Wolfgang, S., and Turkel, E., "Numerical Solution of the Euler Equations by Finite Volume Methods Using Runge Kutta Time Stepping Schemes," AIAA Paper 81-1259, June 1981.

[38]Shmilovich, A., "On Transonic Flow Computations About Airfoils, Axisymmetric Projectiles and Nacelles in Free Air and in Wind Tunnels," Douglas Aircraft Co., MCD Rept. J3852, Huntington Beach, CA, Oct. 1985.

R. M. Cummings
Associate Editor